Pergamon

Int. J. Heat Mass Transfer. Vol. 40, No. 9, pp. 2055–2065, 1997

0017–9310/97 $17.00+0.00

PII: S0017–9310(96)00276–1

The influence of micro-scale solute diffusion and dendrite coarsening upon surface macrosegregation

HÅVARD J. THEVIK and ASBJØRN MO

SINTEF Materials Technology, Box 124 Blindern, 0314 Oslo, Norway

(*Received* 5 *February* 1996 *and in final form* 29 *July* 1996)

Abstract—A model problem and an associated mathematical model relevant for the macrosegregation formation close to and at the surface in aluminium direct chill casting are presented. The model is used to study how the solute diffusion within and coarsening of the dendrites influence the macrosegregation formation due to exudation and solidification shrinkage. It is found that the Scheil limit leads to the thickest and most concentrated exudated layer. For alloys having finite (but slow) solute diffusion, the model predicts a macrosegregation close to that obtained in the lever rule limit. If the secondary dendrite arm spacing is assumed to be equal to that found after complete solidification, the thickness of the exudated layer and the associated solute depletion within the casting are severely overestimated. For cases in which there is no exudation, the positive segregation due to solidification shrinkage is more pronounced the less the local solid solute diffusion is. Coarsening is shown to be of less importance in quantifying the macrosegregation when there is no exudation.

1. INTRODUCTION

Macrosegregation formation, i.e. large (system) scale inhomogeneities in the chemical composition of an alloy, leads to non-uniform product performance and can in severe cases result in product rejection. An important type of macrosegregation is the layer of exudations which often can be seen on the surface of direct chilled (DC) cast aluminium ingots. This exudated layer can be more than 1 mm thick and have a magnesium concentration of 11% when AA5182 rolling slabs with nominal magnesium concentration of 4.7% are cast with the traditional floater regulated technology [1].

Surface exudation is caused by interdendritic melt flow through the mushy zone. The flow is driven by the pressure drop due to air gap formation between the partly solidified shell and the mould [2–6]. The air gap formation furthermore leads to reduced cooling and the mushy shell through which the exudation occurs remelts partially. During DC casting, the surface region also experiences melt flow associated with solidification shrinkage leading to so-called inverse segregation [7–10]. This type of macrosegregation is positive, i.e. the solute concentration becomes larger than the nominal alloying concentration, whereas exudation leads to negative macrosegregation in the region in which interdendritic melt flows [11].

Central to mathematical modelling of macrosegregation is to simultaneously account for the transport of volume averaged (macroscopic) quantities such as mass and enthalpy, and processes occurring on the microscopic scale. More specifically, the macroscopic equations for the mushy zone constituted by a coherent dendritic network surrounded by melt, differ mainly from those for a one phase continuum in that a volume fraction of liquid, g_l, and a permeability, K, appear in the equations. The development of g_l depends on the micro-scale solute diffusion in the solid network, and K, which describes the friction between the solid and the liquid, depends on the fraction of liquid and the microstructural morphology.

This study is directed towards quantifying the effect of the micro-scale phenomena of solute diffusion in the solid and dendrite coarsening on the final macrosegregation. Studies along similar lines can be found in Refs. [12–14] in which the influence of the microstructural development on the macrosegregation is studied in model problems focusing on solidification shrinkage induced flow and/or thermosolutal convection. It is also of interest to note that Glicksman *et al.* [15] coupled a microscopic coarsening theory with an analytical heat-transfer model in predicting dendrite arm spacings. However, in the present paper phenomena associated with the surface segregation problem referred to above, i.e. remelting, exudation and solidification shrinkage induced flow, are addressed in a model problem recently discussed by Haug *et al.* [11].

Mathematical models for solute diffusion and coarsening are presented in Section 2. The model problem and the governing equations are introduced, the numerical solution procedure is outlined, and the solution is compared with other work. In Section 3, the model is used to analyse the effect of the micro-scale transport phenomena upon the macro-scale

NOMENCLATURE

a	parameter in the relation for local solute profile in the solid
b	parameter in the relation for local solute profile in the solid
c	solute concentration
C	specific heat
D	solute diffusivity
f	function for the solid density ($\rho_s = f(c_s, T)$)
g	accelcration duc to gravity; volume fraction (if subscript)
h	specific enthalpy
H	metallostatic head
J	interfacial solute flux due to diffusion
k	partition coefficient
K	permeability; coarsening rate factor (if subscript)
L	length of solution domain
m	slope of the liquidus line
p	liquid pressure
r	distance from the centre of the secondary dendrite arm
S	interfacial area per solid volume; source term in enthalpy conservation (if subscript)
t	time
T	temperature
U	superficial liquid velocity
x	position.

Greek symbols

α	heat transfer coefficient
Δh	specific latent heat
Δr	thickness of exudated layer
Γ	Gibbs–Thomson coefficient
λ	heat conductivity; secondary dendrite arm spacing (if subscript is 2)
μ	dynamic liquid viscosity
ρ	density
$\{\rho c\}$	volumetric solute concentration
$\{\rho h\}$	volumetric enthalpy.

Subscripts

0	surroundings
1	chill contact
2	no chill contact
c	coarsening rate
e	eutectic
i	initial
l	liquid
m	melting point
prev	value from the previous iteration
s	solid
$\{\rho h\}$	enthalpy conservation.

Superscripts

$\overline{\psi}_i$	interfacial average of ψ
$\langle\psi\rangle^s$	intrinsic volume average in the solid of ψ
*	criterion for air gap formation
ex	exudated
p	constant pressure.

transport of solute in a case study involving exudation and in a case study on inverse segregation (no exudation).

2. MATHEMATICAL MODEL

2.1. *Solid solute diffusion*

The volume averaged solute conservation equation of the solid phase can be written as

$$\frac{\partial}{\partial t}(g_s\langle\rho_s c_s\rangle^s) = \overline{c_{si}}\frac{\partial}{\partial t}(g_s\langle\rho_s\rangle^s) + J_s \qquad (1)$$

where t is the time, g_s is the volume fraction of the primary solid phase, ρ_s is the (microscopic) density of the solid, $\langle\ \rangle^s$ represents the intrinsic volume average of the solid, $\overline{c_{si}}$ is the average solid solute concentration at the solid–liquid interface, and J_s is the average interfacial solute flux due to diffusion of solute within the dendrites. The solute diffusion in the solid at the macro-scale has been neglected and the solid phase is stationary and rigid. Notice that equation (1) differs from the corresponding equation in Ni and Beckermann [16, Table 1] in that the present equation accounts for a non-uniform solid density locally. When the diffusion is finite, c_s varies within the dendrites and since ρ_s generally depends on solute concentration, ρ_s will also vary within the dendrites.

In a recent investigation, Combeau *et al.* [17] showed that the solute flux J_s can be adequately modelled by

$$J_s = \frac{36\overline{\rho_{si}}D_s}{\lambda_2^2}(\overline{c_{si}} - \langle c_s\rangle^s) \qquad (2)$$

for both solidification and remelting conditions in an open system.† Here, $\overline{\rho_{si}}$, D_s, and λ_2 are the solid density at the solid–liquid interface, the solute diffusivity in

† The proposed solute flux from Ref. [17] has been slightly modified in order to account for a non-constant solid density.

Table 1. Thermophysical data for Al–4.5%Cu and casting parameters used in the case studies

Symbol	Value	Reference
C_l^p	$1093\ \mathrm{J\ kg^{-1}\ K^{-1}}$	[31]
$C_s^p = C_e^p$†	$1059\ \mathrm{J\ kg^{-1}\ K^{-1}}$	[31]
D_s	$8\times10^{-13}\ \mathrm{m^2\ s^{-1}}$	[32, 33]
k	0.17	[34]
m	-339 K	[34]
T_e	821 K	[34]
T_m	933 K	[34]
Γ	20×10^{-6} m K	[35]
Δh	$400\times10^3\ \mathrm{J\ kg^{-1}}$	[31]
λ_l	$83\ \mathrm{W\ m^{-1}\ K^{-1}}$	[31]
$\lambda_e = \lambda_s$†	$192\ \mathrm{W\ m^{-1}\ K^{-1}}$	[31]
μ	$3\times10^{-3}\ \mathrm{kg\ m^{-1}\ s^{-1}}$	[31]
ρ_l	$1000/[0.3970-0.45322c_l+4.0924\times10^{-5}(T-273.15)+1.1078\times10^{-4}c_l(T-273.15)+0.27475c_l^2]\ \mathrm{kg\ m^{-3}}$	[25]
ρ_s	$1660531/\{(9.26612-5.33221c_s)[4.00451-0.53092c_s/(2.35545-1.35545c_s)+1.2737\times10^{-4}T]^3\}$;	present work
ρ_e	$3409\ \mathrm{kg\ m^{-3}}$	[25]
c_i	4.5%	
g_l^*	0.19	[1]
H	0.08 m	
L	0.15 m	
T_0	293 K	
T_i	973 K	
α_1	$1000\ \mathrm{W\ m^{-2}\ K^{-1}}$	
α_2	$300\ \mathrm{W\ m^{-2}\ K^{-1}}$	

†Thermophysical properties of the eutectic are set equal to those of the primary solid phase.

the solid, and the secondary dendrite arm spacing, respectively. This expression for J_s is based on the following assumptions [17]: (1) the solid is present as a regular array of cylinders, i.e. cylindrical morphology (corresponding to the microstructure assumed in the coarsening model, see Section 2.2); (2) the solute concentration locally in the dendrites is given by $c_s = ar^5 + b$, where r is the distance from the centre of the secondary dendrite arm, and a and b are parameters determined by c_s and $\overline{c_{si}}$; (3) $\overline{c_{si}} = kc_l$ during both solidification and remelting, where k is the partition coefficient and c_l the liquid solute concentration (which in the present study is uniform locally).

The solute conservation of the solid obtained by inserting equation (2) into equation (1) has two quantities which can be regarded as unknown variables, namely $\langle\rho_s c_s\rangle^s$ and $\langle c_s\rangle^s$. In the Scheil limit, i.e. no solute diffusion in the solid ($D_S = 0$), this does not pose any problem because the solute profile is "frozen" and as shown by Voller and Sundarraj [13], the local variation in ρ_s can then be accounted for. However, in the general case of finite solute diffusion, we propose to resolve this problem with the following three approximations: (1) $\langle\rho_s c_s\rangle^s = \langle\rho_s\rangle^s\langle c_s\rangle^s$; (2) given that $\rho_s = f(c_s, T)$ where f is some function and T is the (uniform) temperature in the averaging volume, $\langle\rho_s\rangle^s = f(\langle c_s\rangle^s, T)$; (3) $\overline{\rho_{si}}$ in equation (2) is substituted with $\langle\rho_s\rangle^s$. In the remaining of the paper, the bracket symbolizing an intrinsic volume average is dropped ($\langle c_s\rangle^s \to c_s$ etc.), and the macroscopic solute conservation of the solid phase can now be written as

$$\frac{\partial}{\partial t}(g_s\rho_s c_s) = \overline{c_{si}}\frac{\partial}{\partial t}(g_s\rho_s) + \frac{36\rho_s D_s}{\lambda_2^2}(\overline{c_{si}} - c_s). \quad (3)$$

2.2. *Dendrite coarsening*

We employ the model developed by Mortensen [18] for describing the coarsening of the primary solid phase. This model accounts for differences in the coarsening rate depending on the local temperature and liquid fraction, cf. the experimental observations in Refs. [19, 20]. Mortensen neglected coarsening due to coalescence and derived the following expression for the development of the secondary dendrite arm spacing

$$\frac{d\lambda_2}{dt} = \frac{1}{3\lambda_2^2}\frac{27\Gamma D_l}{4(1-k)(1-g_l)(1-\sqrt{1-g_l})(T_m - T)} \equiv \frac{K_c(g_l, T)}{3\lambda_2^2}. \quad (4)$$

Here, Γ is the Gibbs–Thomson coefficient, D_l the solute diffusivity in the liquid, g_l the volume fraction of liquid, and T_m the melting point of pure aluminium. Furthermore, K_c is referred to as the coarsening rate factor. The development of equation (4) is based on the assumption of a cylindrical geometry of the secondary dendrite arms.

In the case studies to be presented in Section 3 we use the Kozeny–Carman relation for the permeability K

$$K = \frac{g_l^3}{5S^2(1-g_l)^2} \quad (5)$$

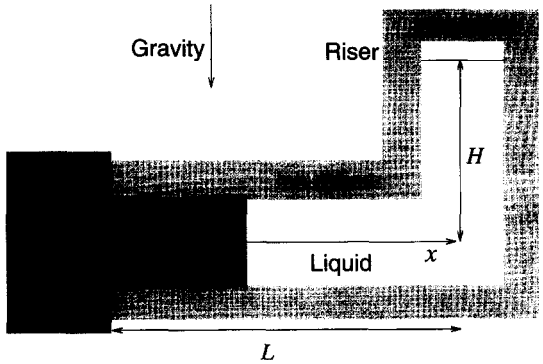

Fig. 1. The model problem.

where S is the solid–liquid interfacial area per volume of solid. Since we have chosen λ_2 to "represent" the length of the microstructure, a relation between S and λ_2 is needed. For cylindrical secondary dendrite arms of uniform width surrounded by liquid, the average diameter D of a secondary dendrite arm is related to the average secondary dendrite arm spacing λ_2 by $D = \lambda_2\sqrt{1-g_l}$ [18]. Furthermore, the solid–liquid interfacial area per volume of solid is related to the dendrite diameter by $S = 4/D$ when the top of the cylinder/secondary dendrite arm is neglected [21]. This gives

$$S = \frac{4}{\lambda_2\sqrt{1-g_l}} \tag{6}$$

and by combining equations (5) and (6), the permeability can be written as

$$K = \frac{\lambda_2^2}{80}\frac{g_l^3}{1-g_l}. \tag{7}$$

2.3. *Model problem*

As discussed by Haug *et al.* [11], the main mechanisms causing macrosegregation close to the surface in DC-casting are exudation and solidification shrinkage.† In the present work a model problem similar to that of Ref. [11] is used to study how finite solute diffusion in the solid and coarsening affects the macrosegregation development close to the surface.

Taking x to be the spatial coordinate in the one dimensional model problem shown in Fig. 1, the surface at $x = 0$ can either be in contact with the chill or there can be a situation in which the semi-solid shell has contracted from the chill. In the latter case interdendritic liquid can exude at the surface (if the liquid fraction at $x = 0$ is non-zero).

The conservation equations for mass, momentum, enthalpy and solute are similar to those of Ref. [11], with the exception that the energy conservation is formulated in terms of the enthalpy instead of the temperature, i.e.

$$\frac{\partial\rho}{\partial t} + \frac{\partial}{\partial x}(\rho_l U_l) = 0 \tag{8}$$

$$\frac{\mu}{K}U_l + \frac{\partial p}{\partial x} = 0 \tag{9}$$

$$\frac{\partial}{\partial t}\{\rho h\} + \frac{\partial}{\partial x}(\{\rho h\}U_l) = \frac{\partial}{\partial x}\left[\frac{\lambda}{C_s^p}\frac{\partial}{\partial x}\left(\frac{\{\rho h\}}{\rho}\right)\right] + S_{\{\rho h\}} \tag{10}$$

$$\frac{\partial}{\partial t}\{\rho c\} + \frac{\partial}{\partial x}(\rho_l c_l U_l) = 0. \tag{11}$$

Here, ρ, ρ_l, U_l, μ and p are the density of the two-phase averaging volume, liquid density, superficial liquid velocity, dynamic viscosity and pressure, respectively. Furthermore, $\{\rho h\}$, λ, C_s^p, $S_{\{\rho h\}}$ and $\{\rho c\}$ are the enthalpy per volume, effective heat conductivity, specific heat of the solid, source term in the enthalpy balance and solute mass per volume, respectively. The product of ρ and h (h being the enthalpy per mass of the two-phase material) is regarded as a primary unknown in the numerical solution procedure and is therefore written as $\{\rho h\}$ in equation (10). Also the solute mass per volume, $\{\rho c\}$, is regarded as a primary unknown.

The model is closed by the following relations:

$$\rho = g_l\rho_l + g_s\rho_s + g_e\rho_e \tag{12}$$

$$\{\rho h\} = (g_l\rho_l C_l^p + g_s\rho_s C_s^p + g_e\rho_e C_e^p)T + g_l\rho_l\Delta h \tag{13}$$

$$\lambda = g_l\lambda_l + g_s\lambda_s + g_e\lambda_e \tag{14}$$

$$S_{\{\rho h\}} = \frac{\partial}{\partial x}\left[\frac{\lambda}{C_s^p}\frac{\partial}{\partial x}\left(C_s^p T - \frac{\{\rho h\}}{\rho}\right)\right] - \frac{\partial}{\partial x}\{[\rho_l(C_l^p T + \Delta h) - \{\rho h\}]U_l\} \tag{15}$$

$$\{\rho c\} = g_l\rho_l c_l + g_s\rho_s c_s + g_e\rho_e c_e \tag{16}$$

$$1 = g_l + g_s + g_e \tag{17}$$

$$c_l = (T - T_m)/m \quad \text{when} \quad 0 < g_l < 1 \tag{18}$$

$$\overline{c_{si}} = kc_l \quad \text{when} \quad 0 < g_l < 1 \tag{19}$$

$$g_e = 0 \quad \text{when} \quad T > T_e \tag{20}$$

$$\frac{\partial g_s}{\partial t} = 0 \quad \text{when} \quad T = T_e. \tag{21}$$

Here, g_e, ρ_e, Δh, c_e, m, k and T_e are the volume fraction of eutectic, density of the eutectic solid, latent heat, eutectic concentration, slope of the liquidus line, partition coefficient, and eutectic temperature, respectively. Furthermore, C_l^p and C_e^p are the specific heat of the liquid and eutectic, and λ_l, λ_s and λ_e are the

† It has recently been shown by Schneider and Beckermann [14] that macroscopic solute diffusion in the liquid leads to an extremely narrow negatively segregated band close to the chill. The effect of the macroscopic liquid solute diffusion is discussed in Ref. [22, Paper 6], and there it is shown that this effect does not significantly change the inverse segregation profile for $x > 200$ μm (for the alloy and casting parameters in Table 1).

heat conductivity of the liquid, solid and eutectic, respectively. It should be noted that since the volume fraction of the primary phase is assumed not to change during the eutectic reaction (cf. equation (21)) while c_s increases due to the solute diffusion, equation (16) implies that c_e will deviate slightly from the eutectic liquid concentration. This paradoxical result is due to equation (21). Allowing g_s to change during the eutectic solidification would only have a marginal effect in the case studies discussed in Section 3.

The boundary conditions at $x = 0$ reflect zero normal velocity (no exudation) when there is chill contact, and atmospheric pressure, p_0, when the mould is removed (thereby neglecting any influence of the oxide layer and capillary effects at the surface upon the exudation). The different surface cooling associated with these two conditions are expressed in a relatively high heat transfer coefficient, α_1, when there is chill contact, and a low heat transfer coefficient, α_2, when there is no contact (see Table 1). At $x = L$, there is no diffusive transport of energy into the system and there is an overpressure due to the metallostatic head. Mathematically this can be summarized as

$x = 0$:

$$\begin{cases} U_l = 0, & \lambda \dfrac{\partial T}{\partial x} = \alpha_1 (T - T_0) \quad \text{if chill contact} \\ p = p_0, & \lambda \dfrac{\partial T}{\partial x} = \alpha_2 (T - T_0) \quad \text{if no chill contact} \end{cases} \tag{22}$$

$$x = L: \quad p = p_0 + \rho_l g H, \quad \frac{\partial T}{\partial x} = 0 \tag{23}$$

where T_0 and g are the temperature of the surroundings at $x = 0$ and the gravity constant, respectively.

The exudation can be characterized by the thickness, Δr, and the average solute concentration, c^{ex}, of the surface layer. These quantities are given by

$$\Delta r = \left| \int_0^t U_l(x = 0, \hat{t})\, \mathrm{d}\hat{t} \right| \tag{24}$$

$$c^{ex} = \frac{\displaystyle\int_0^t c_l(x = 0, \hat{t}) U_l(x = 0, \hat{t})\, \mathrm{d}\hat{t}}{\displaystyle\int_0^t U_l(x = 0, \hat{t})\, \mathrm{d}\hat{t}}. \tag{25}$$

Initially, the temperature and solute concentration distributions are taken to be uniform and equal to T_i and c_i, respectively. Furthermore, at the start of the calculations liquid at rest occupies the solution domain. Following the work of Mortensen [18], coarsening is neglected in the initial stages of the solidification. In the present model, the secondary dendrite arm spacing is assumed to be 3 μm when $g_l > 0.9$. It should be noted that the results are insensitive to the initial λ_2; choosing any initial value between 0.1 μm and 10 μm does not alter the results significantly.

2.4. *Solution procedure*

During chill contact the velocity can be calculated from the mass conservation (8) without invoking the momentum equation (9) because the solidification is unidirectional and there is no pore formation. When there is no chill contact, a pressure equation is obtained by combining equations (8) and (9)

$$\frac{\partial}{\partial x}\left(\rho_l K \frac{\partial p}{\partial x}\right) = \mu \frac{\partial \rho}{\partial t}. \tag{26}$$

Equations (1), (8)–(11) and (26) have been spatially discretized by a control-volume based finite difference procedure and an implicit scheme is adopted for the time integration. The velocities close to the surface due to the solidification shrinkage are small, i.e. $\Delta x \gg V \Delta t$, where Δx, V and Δt are the length of the control volume, a representative velocity and the time increment, respectively, and the convective terms in the enthalpy and solute conservation equations have therefore been discretized using a central-difference approach. The resulting set of differential equations has been solved sequentially.

Given that all quantities at the previous time step are known, the solution algorithm for finding the unknowns at the new time step is:

(1) $\{\rho h\}$ is found from equation (10) by using previous values for U_l, λ, ρ and $S_{\{\rho h\}}$.

(2) With the new $\{\rho h\}$ and $\{\rho c\}$ from the previous iteration, c_s, g_l, g_s, g_e and T are found by:

  (a) With the previous values for c_s, equations (12)–(21) are used to find g_l, g_s, g_e and T.

  (b) For finite values of the solute diffusivity in the solid, c_s is found by solving the solid solute conservation equation (3) using g_s and $\overline{c_{si}} = k c_l(T)$ from step 2(a). Notice that since the solute diffusion is zero in the Scheil limit, it follows that solute conservation equation simplifies allowing c_s to be easily updated from equation (3). In the lever rule limit ($D_s \to \infty$), equation (3) does not need to be solved because the solid concentration is related to the liquid concentration by $c_s = k c_l$.

  (c) The densities ρ_l, ρ_s, ρ_e and ρ are updated using T, c_l and c_s from steps 2(a) and 2(b) and the relations listed in Table 1.

  (d) Steps 2(a–c) are repeated until the relative difference between the iterations becomes less than a small number, i.e.

$$\frac{\max(|T - T_{prev}|)}{\max T} + \frac{\max(|g_l - g_{l,prev}|)}{\max g_l} + \frac{\max(|c_s - c_{s,prev}|)}{\max c_s} \leqslant 5 \times 10^{-4} \tag{27}$$

where the subscript prev represents the value at the previous iteration.

(3) The secondary dendrite arm spacing is updated by direct integration of equation (4). The integral $\int_{t_{prev}}^{t} K_c(g_l, T)\,dt$ is evaluated by the midpoint rule using new values for g_l and T from step 2.

(4) In case of chill contact, U_l is found from equation (8). When there is no chill contact, equation (26) is used to calculate the pressure, and the velocity can then be solved from equation (9). In either case, the new values for g_l, ρ_l and ρ from step 2 are used in the calculations.

(5) $\{\rho c\}$ is calculated from equation (11) using ρ_l and $c_l = c_l(T)$ from step 2, and U_l from step 4.

(6) The effective heat conductivity and the source term in the enthalpy conservation (10) are updated.

Steps 1–6 are repeated until

$$\frac{\max(|\{\rho h\} - \{\rho h\}_{prev}|)}{\max\{\rho h\}} + \frac{\max(|\{\rho c\} - \{\rho c\}_{prev}|)}{\max\{\rho c\}} \leqslant 10^{-3}. \quad (28)$$

The time step is doubled if steps 1–6 converge after one iteration and the time step is reduced by half if equation (28) cannot be satisfied after 10 iterations.

In step 3 above, we note that equation (4), which describes the evolution of λ_2, is integrated for liquid fractions from 0.9 to 0.07 [18]. Moreover, modelling solid contraction in the completely solidified region is not a part of the present study. Therefore, ρ_s at positions where $g_l = 0$ corresponds to the solid density at the time when the control volume solidified completely.

The boundary conditions for the energy, equations (22) and (23), have been reformulated to

$$\lambda \frac{\partial}{\partial x}\left(\frac{\{\rho h\}}{\rho}\right) = \alpha\left(\frac{\{\rho h\}}{\rho} - C_s^p T_0\right) + \left(\alpha - \lambda\frac{\partial}{\partial x}\right)\left(C_s^p T - \frac{\{\rho h\}}{\rho}\right). \quad (29)$$

The last term on the right-hand-side of this equation has been treated as a source similarly to $S_{\{\rho h\}}$ in equation (10), while the term on the left-hand-side and the first term on the right-hand-side of equation (29) have been discretized implicitly in time and imposed into the general scheme obtained from discretizing equation (10).

The solution algorithm has been implemented in MATLAB [23]. Using 300 grid points and an initial time step of 0.05 s (the time step increases towards the end of the solidification) result in a CPU time of 8.5 h and 5 h on a Hewlett-Packard-9000-735 workstation for the exudation cases in Section 3.1 and the inverse segregation cases in Section 3.2, respectively.

2.5. *Comparison with other work*

The present model has been compared with the models of Haug *et al.* [11] and Thevik and Mo [21] and nearly identical results are obtained. Also the analytical expressions for the inverse segregation and the eutectic fraction derived in Ref. [22, Paper 2] have been used to verify the present program code. Assuming $\rho_l = 2480$ kg m^{-3}, $\rho_s = 2703$ kg m^{-3}, and otherwise using data material data for Al–4.5%Cu and the casting parameters of Table 1, the modelling results and the analytical predictions are summarized in Table 2 (the concentration at the surface for the present model is found by linearly extrapolating the solute concentration values in the two nearest control volumes). There is close correspondence between the present numerical results and the analytical ones calculated from Ref. [22, Paper 2].

Kato and Cahoon [24] measured the inverse segregation in an Al–4.1%Cu alloy. Assuming the effective heat transfer coefficient during the experiment to be $\alpha_l = 1684.21 - 4.3443t + 0.00449561t^2$ W m^{-2} K^{-1} [13], where t is in seconds, using $L = 0.1323$ m, $T_i = 1020$ K and otherwise using the data in Table 1, the final solute distribution predicted by the present model is compared with the experimental data in Fig. 2. It can be seen that the present model gives results in reasonable agreement with the measured values.

It should be noted that the relation for the solid density, cf. Table 1, is derived from the lattice parameter relation in Ref. [25, equation 3] and the fact that there are four atoms in a unit cell (fcc crystal lattice and a negligible number of interstitial atoms). This relation is generally applicable since it depends on the average solid concentration and the temperature. The inverse segregation profile in Voller and Sundarraj [13] (in the limit of no pore formation) is also shown in Fig. 2. The much lower macro-

Table 2. Comparison of the final solute concentration and eutectic fraction at the chill face for an inverse segregation case

	c [%Cu]		g_e [%]	
D_s	Present model	Analytical model (Ref. [22, Paper 2])	Present model	Analytical model (Ref. [22, Paper 2])
0	5.168	5.167	11.00	11.05
∞	4.974	4.973	0	0

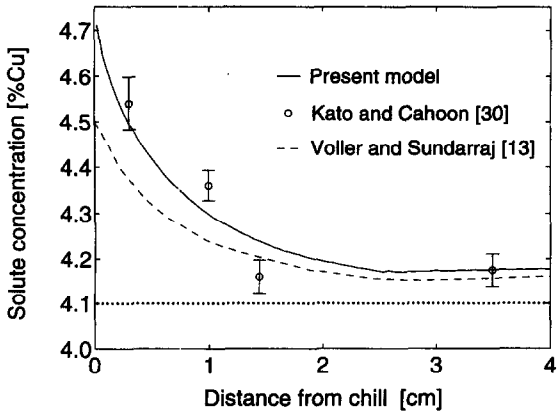

Fig. 2. Comparison between measured and calculated inverse segregation.

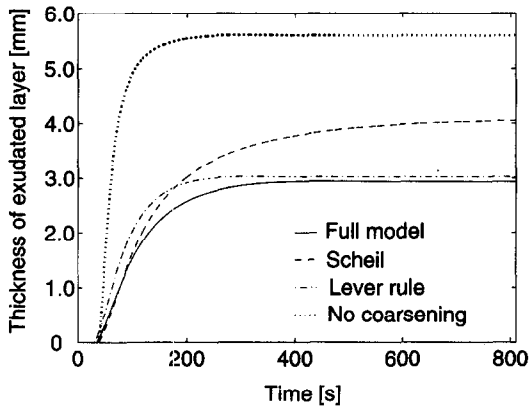

Fig. 3. The thickness of the exudated layer vs time.

segregation predicted in Ref. [13] compared to the present work is mainly due to differences in the density models [26] (a discussion on the effect of different density models upon the inverse segregation can be found in Ref. [27]).

3. RESULTS AND DISCUSSION

3.1. *Exudation*

The material data and casting parameters used in the model problem are given in Table 1. In the initial stages of solidification, there is chill contact. When the liquid fraction becomes less than some critical value, g_l^*, at $x = 4.5$ mm from the chill [1, 6, 28], the chill is removed and interdendritic liquid exudes onto the casting surface. Associated with the chill removal is a substantial decrease in the heat transfer coefficient. This leads to partial remelting of the mushy zone close to the chill, and amplifies the extent of exudation [11].

The development of the exudated layer is shown in Fig. 3 for four different cases. The solid line represents the prediction when both finite solute diffusion within the dendrites and coarsening of the microstructure are accounted for. This case is referred to as the "full model". Then there are two cases referred to as "Scheil" and "Lever rule" which are similar to the full model except that there are zero and infinite micro-scale solute diffusion in the solid, respectively.†

Table 3. Data for the exudated layer

Case study	Δr [mm]	c^{ex} [% Cu]
Full model	2.9	14.1
Scheil	4.1	16.3
Lever rule	3.0	12.8
No coarsening ($\lambda_2 = 98$ μm)	5.6	12.5

The fourth case, labelled "no coarsening", is similar to the full model except that the secondary dendrite arm spacing is taken to be constant in both time and space. In this case, λ_2 is assigned the value 98 μm, which corresponds to the final λ_2 predicted by the full model and averaged over the interval $0 < x < 6$ cm. The thickness and the average solute concentration of the exudated layer in the four cases are summarized in Table 3, and the solute concentration after complete solidification is shown in Fig. 4.

3.1.1. *Effect of solute diffusion in the dendrites.* From Fig. 3 it can be seen that the full model and the lever rule predict exudated layers of nearly the same thickness. The Scheil limit leads to a Δr being about 40% thicker. The reason for these differences is that the liquid fraction development depends on the extent of local solute diffusion. The liquid fraction and the temperature at $x = 0$ have been plotted as a function of time in Fig. 5. This figure reveals that the increase in g_l due to the reheating associated with the air gap

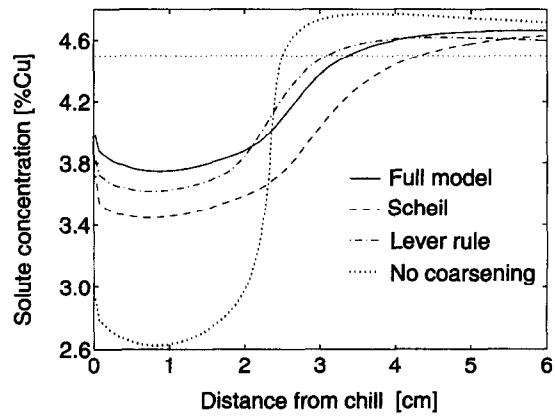

Fig. 4. The solute concentration after complete solidification vs the distance from the chill.

† From a microscopic point of view, the Scheil limit can be associated with a "frozen" solute profile in the dendrite arms. During solidification this is simply modelled by setting $D_s = 0$ in equation (3). However, in a remelting situation in which c_l and c changes, the assumption of thermodynamical equilibrium at the interface (cf. equation (19)) is not necessarily fulfilled [17, 29, 30]. Consequently, what is referred to as the "Scheil limit" in the present paper (i.e. $D_s = 0$ in equation (3) and equation (19) being valid) can, if c changes in a remelting situation, be associated with a minor modification of the "frozen" profile.

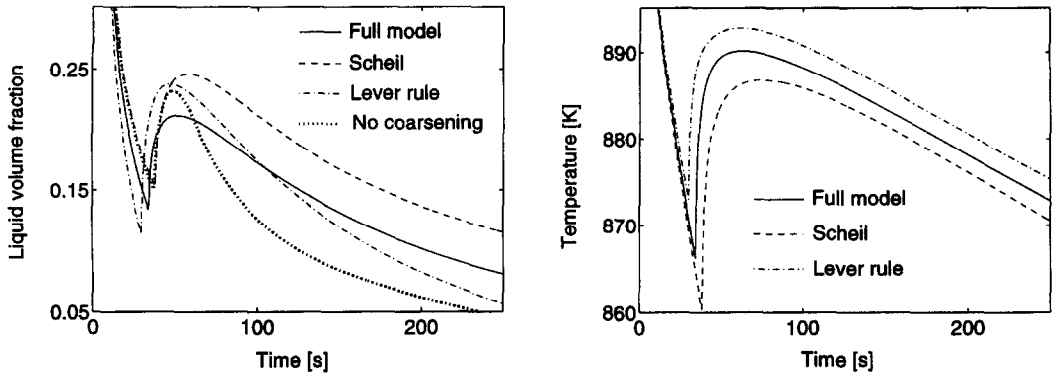

Fig. 5. Evolution of the liquid fraction (a) and the temperature (b) at $x = 0$.

formation is considerably less for the full model than it is for the lever rule and the Scheil limit.

By comparing the results of the full model with the lever rule results, it is seen that the liquid fraction is greater in the lever rule case between 30–100 s. Although g_l in the full model becomes larger than the liquid fraction in the lever rule case after about 100 s, the major part of the exudation takes place during the first seconds after the chill removal and Δr for the lever rule therefore becomes somewhat greater. The extent of exudation is greatest in the Scheil case because the liquid fraction is significantly greater than in the other cases after about 60 s. Furthermore, it takes a much longer time before the surface solidifies in the Scheil case than in the full model and lever rule cases. This means that the mushy zone extends furthest into the casting during the exudation for the Scheil case. Correspondingly, the solute depleted zone (i.e. the region having $c < c_0$) is therefore the widest in the Scheil case; see Fig. 4. Notice also from Table 3 that there is a significant difference in the concentration of the exudated layer. Since c_{ex} depends on the liquid solute concentration at the surface (see equation (25)), and the temperature at $x = 0$ is lowest for the Scheil case (see Fig. 5(b)), c_{ex} becomes highest in the Scheil limit.

In order to elucidate the effect of micro-scale solute diffusion, the temperature versus liquid fraction (i.e. the solidification path) at the surface has been plotted in Fig. 6(a) (the reason for the solidification paths of the lever rule and Scheil limits not being simple, smooth curves is that the solute concentration is not constant). Before the chill is removed, it is seen that the full model leads to a solidification path approximately midway between the Scheil and lever rule limits. However, during the remelting the full model approaches the lever rule curve. This behaviour can be related to the diffusive interfacial flux, J_s, shown in Fig. 6(b).† This figure reveals that before the remelting, the solute flux is highest for the lever rule, J_s for the full model has half the value of the lever rule, and the diffusive solute flux is zero in the Scheil limit. This picture changes significantly when the alloy starts to remelt. While the interfacial diffusive flux remains positive during most of the remelting for the full model, J_s is proportional to $-\partial T/\partial t$ in the lever rule limit leading to a large negative solute flux. When the remelting ceases and the alloy starts to resolidify, the solute fluxes for the full model and the lever rule become positive again. Notice from Fig. 6(b) that due to the low heat transfer coefficient associated with the air gap and the resulting small solidification rate, J_s approaches the lever rule value during the last part of the solidification. This implies that the alloy at $x = 0$ solidifies above the eutectic temperature for the full model, while g_e is close to 0.05 in the Scheil limit; see Fig. 6(a).

In essence, for intermediate values of D_s in a remelting case, it takes some time to change the monotonically increasing solute profile in the dendrites associated with the (initial) solidification, to a situation having $c_s > kc_l$ which leads to a negative J_s, see equation (2). This means that the solute concentration in the solid can increase even during remelting, leading to a smaller g_l and thereby less exudation.

3.1.2. *Effect of dendrite coarsening.* The case with no coarsening, i.e. $\lambda_2 = 98$ μm (λ_2 is uniform and constant), results in the thickest exudated layer (see Fig. 3) and the most pronounced solute depletion within the casting (see Fig. 4). This is related to the development of the secondary dendrite arm spacing displayed in Fig. 7(a), which shows that λ_2 is less than 98 μm during the exudation. Since the permeability is proportional to λ_2^2 (see equation (7)), the permeability, and therefore also the exudation, is less in the cases accounting for the coarsening compared to the case with $\lambda_2 = 98$ μm. It is also seen from Fig. 3 that the very rapid increase in Δr just after the chill removal ceases after approximately 100 s in the case with no coarsening. From then on the thickness of the exudated layer increases much less than in the cases accounting for coarsening. The reason for this is that the large flow rate in the case with no coarsening leads

† The flux is calculated by $J_s = g_s\rho_s(\partial c_s/\partial t) = g_s\rho_s(k/m)(\partial T/\partial t)$ in the lever rule limit.

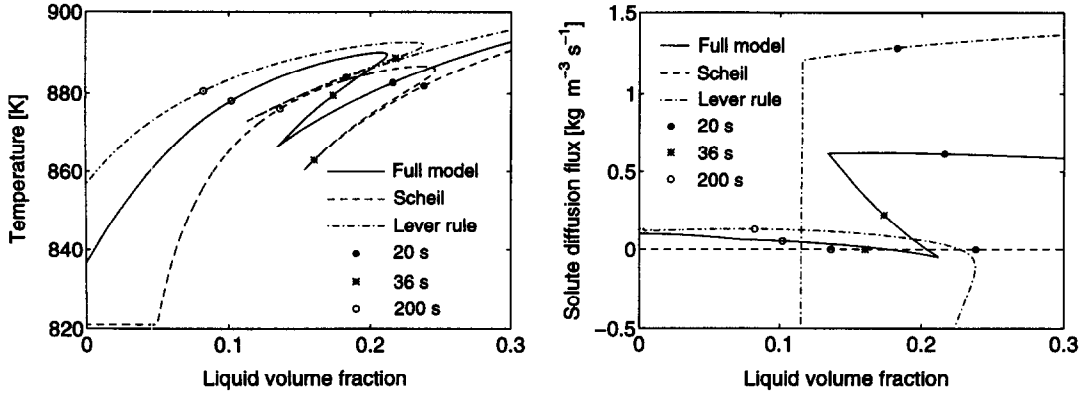

(a) (b)

Fig. 6. The temperature (a) and the interfacial solute flux due to diffusion (b) vs the liquid fraction at $x = 0$.

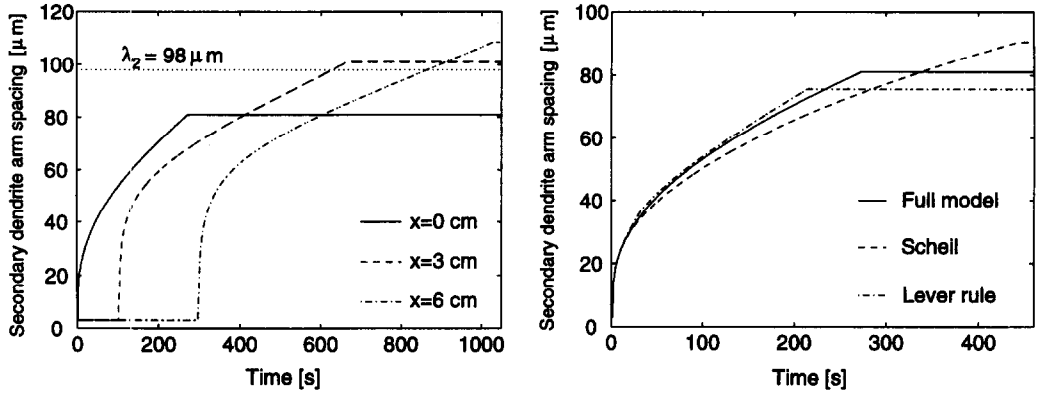

(a) (b)

Fig. 7. (a) The evolution of λ_2 at three spatial positions; (b) the evolution λ_2 at the surface for the full model, lever rule and Scheil limit.

to a pronounced negative macrosegregation (decrease in c) and thereby so-called constitutional solidification; see Fig. 5(a). The resistance towards flow therefore increases. The fact that the exudation is negligibly small after about 200 s results in a more narrow solute depleted zone in the no coarsening case compared with the other cases; see Fig. 4.

From the above discussion it is apparent that assuming λ_2 to be (nearly) equal to the secondary dendrite arm spacing after complete solidification, overestimates the macrosegregation formation. As discussed in Ref. [21], it is possible to find a "representative", constant value of λ_2 which gives reasonable correspondence with the final macrosegregation obtained with the full model. However, such a constant value for the secondary dendrite arm spacing is not known *a priori*.

Since the secondary dendrite arm spacing is an important parameter in characterizing a cast alloy, it is of interest to investigate how the solute diffusion influences the coarsening. The evolution of λ_2 at the surface for the full model, lever rule and Scheil limit are displayed in Fig. 7(b). The differences in λ_2 after complete solidification are mainly due to the different solidification times. The less the extent of solute diffusion in the dendrites is, the longer is the solidification time, and thereby λ_2. However, even before the lever rule curve reaches its plateau in Fig. 7(b), λ_2 evolves differently in the three cases. This can be related to the coarsening rate factor K_c and its dependency on the liquid fraction and temperature (cf. equation 4). As shown in Fig. 5, there are substantial differences in g_l and T for the full model, lever rule and Scheil limit after about 40 s, and this corresponds to the time when the growth rate of λ_2 starts to differ significantly for the three cases in Fig. 7(b).

3.2. *Inverse segregation*

In the inverse segregation case study (no exudation), the alloy is always in contact with the chill, and the heat transfer coefficient is equal to $\alpha_1 = 1000\ \mathrm{W\ m^{-2}\ K^{-1}}$ at all times. Four cases similar to those in the exudation case study are discussed, the only difference being that $\lambda_2 = 55\ \mu\mathrm{m}$ for the case with no coarsening which corresponds to the average of the final λ_2 in the interval $0 < x < 6$ cm. The solute

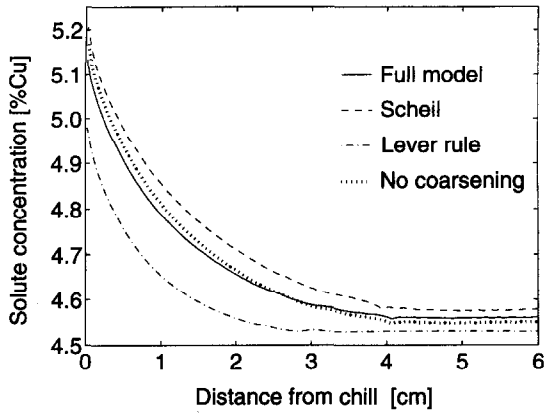

Fig. 8. Final solute concentration versus distance from chill.

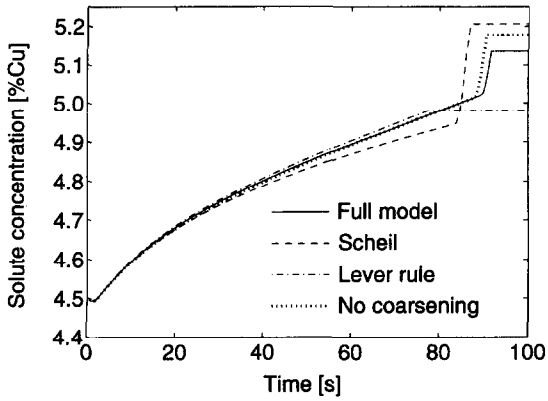

Fig. 9. The evolution of the solute concentration at $x = 0$.

concentration after complete solidification is shown in Fig. 8. The Scheil and no coarsening cases give a segregation profile close to that of the full model. However, the lever rule case differs somewhat more from the full model, and this can be explained from the development of the total concentration shown in Fig. 9. During the eutectic reaction there is a large increase in the total density of a solidifying volume element because the density of the eutectic solid phase is very high; see Table 1. This implies that the solute concentration also increases significantly during the eutectic solidification and from Fig. 9 it can be seen that nearly 40% of the inverse segregation for the Scheil limit can be associated with the eutectic solidification (the eutectic fraction is 0.088). For the lever rule case, the total concentration is less than $kc_e = 5.6\%$Cu, which implies that the eutectic fraction is zero and the final solute concentration becomes less.

The results illustrated in Fig. 8 emphasize the importance of employing a density model which predicts physical results independently of the micro-scale solute diffusion model. The density model in the inverse segregation study in Ref. [12] gave positive segregation with finite and zero micro-scale diffusion, and in the lever rule limit a negative segregation was predicted in a region 0.5 cm from the surface.

Whether or not coarsening is taken into account, is of less importance in the inverse segregation study compared to the exudation study (see Figs. 4 and 8). The secondary dendrite arm spacing represents a measure of the micro-scale characteristic length and influences the extent of solute diffusion in the dendrites, thereby also influencing the development of g_l. This effect is present in both the exudation cases and the inverse segregation cases. However, since the velocity can be calculated from the mass conservation, equation (8), without invoking the momentum, equation (9), the influence of the secondary dendrite arm spacing upon the permeability does not affect the solute concentration in the inverse segregation case. The marginally higher solute concentration of the no coarsening case compared with the full model for $x \leqslant 2.5$ cm, is due to the fact that $\lambda_2 = 55\ \mu$m is greater than the secondary dendrite arm spacing in the full model. This implies that the diffusive solute flux into the solid is greater in the full model (see equation (2)), leading to a slightly smaller eutectic fraction and inverse segregation in the full model ($g_e = 0.034$ and $g_e = 0.051$ for the full model and no coarsening case, respectively). It should be noted that in Ref. [12], coarsening was shown to have an effect on the inverse segregation even in the Scheil limit. However, the present model shows that this cannot be the case since J_s then is zero independently of λ_2 (see equation (2)).

4. CONCLUSION

In a model problem relevant for the surface region in aluminium DC casting, the effect of micro-scale solute diffusion in the solid and of dendrite coarsening upon the macrosegregation formation has been studied.

- The exudation phenomenon is most pronounced in the case of no solute diffusion within the dendrites. For alloys having slow, finite micro-scale solute diffusion in the solid (e.g. Al–Cu alloys), the final macrosegregation can become close to that obtained in the lever rule limit.
- The thickness of the exudated layer and the extent of solute depletion near the chill are overestimated if the secondary dendrite arm spacing is assumed to be constant and equal to the final secondary dendrite arm spacing.
- When there is no exudation, the positive segregation close to the chill due to solidification shrinkage becomes greater the less the micro-scale solid solute diffusion is. Coarsening has a minor influence on the final solute concentration profile.

Acknowledgements—This research was supported by The Norwegian Research Council through program no. 100998/420: Simulation of Multiphase Flow. The authors thank Dr Jane Thatcher for proofreading the manuscript.

REFERENCES

1. Mo, A., Johnsen, T. E., Henriksen, B. R., Jensen, E. K. and Myhr, O. R., Modelling the surface segregation

development in DC casting. In *Light Metals*, ed. U. Mannweiler. Warrendale, PA, 1994, TMS-AIME, pp. 889–896.
2. Emley, E. F., Continuous casting of aluminium. *International Metals Reviews*, 1976, pp. 75–115.
3. Buxmann, K., Mechanismen der Oberflächenseigrung von Strangguß. *Metallurgica*, 1977, **31**(2), 163–170.
4. Ohm, L. and Engler, S., Treibende Kräfte der Oberflächenseigrungen beim NE-Stranguß. *Metallurgica*, 1989, **43**(6), 520–524.
5. Mo, A., Mathematical modelling of surface segregation in aluminium DC casting caused by exudation. *International Journal of Heat and Mass Transfer*, 1993, **36**(18), 4335–4340.
6. Henriksen, B. R. and Jensen, E. K., Modelling the effect of casting speed and metal level on the surface segregation of AA5182. In *Light Metals*. Warrendale, PA, 1993, TMS-AIME.
7. Flemings, M. C. and Nereo, G. E., Macrosegregation, Part I. *Transactions of Metallurgical Society of AIME*, 1967, **239**, 1449–1461.
8. Minakawa, S., Samarasekera, I. V. and Weinberg, F., Inverse segregation. *Metallurgical Transactions*, 1985, **16B**, 595–604.
9. Diao, Q. Z. and Tsai, H. L., Modelling of solute redistribution in the mushy zone during solidification of aluminium-copper alloys. *Metallurgical Transactions*, 1993, **24A**, 963–973.
10. Chen, J. H. and Tsai, H. L., Inverse segregation for a unidirectional solidification of aluminium–copper alloys. *International Journal of Heat Mass Transfer*, 1993, **36**(12), 3069–3075.
11. Haug, E., Mo, A. and Thevik, H. J., Macrosegregation near a cast surface caused by exudation and solidification shrinkage. *International Journal of Heat and Mass Transfer*, 1995, **38**(9), 1553–1563.
12. Sundarraj, S. and Voller, V. R., A dual scale model of segregation phenomena. *ASME Transport Phenomena in Solidification*, 1994, **HTD-284**, 29–42.
13. Voller, V. R. and Sundarraj, S., A model of inverse segregation: the role of microporosity. *International Journal of Heat and Mass Transfer*, 1995, **38**(6), 1009–1018.
14. Schneider, M. C. and Beckermann, C., A numerical study of the combined effects of microsegregation, mushy zone permeability and flow, caused by volume contraction and thermosolutal convection, on macrosegregation and eutectic formation in binary alloy solidification. *International Journal of Heat and Mass Transfer*, 1995, **38**(18), 3455–3473.
15. Glicksman, M. E., Smith, R. N., Marsh, S. P. and Kuklinski, R., Mushy zone modelling with microstructural coarsening kinetics. *Metallurgical Transactions*, 1992, **23A**, 659–667.
16. Ni, J. and Beckermann, C., A volume-averaged two-phase model for transport phenomena during solidification. *Metallurgical Transactions*, 1991, **22B**, 349–361.
17. Combeau, H., Drezet, J.-M., Mo, A. and Rappaz, M., Modelling of microsegregation in macrosegregation computations. *Metallurgical and Materials Transactions A*, 1996, **27A**, 2314–2327.
18. Mortensen, A., On the rate of dendrite arm coarsening. *Metallurgical Transactions*, 1991, **22A**, 569–574.
19. Kattamis, T. Z., Coughlin, J. C. and Flemings, M. C., Influence of coarsening on dendrite arm spacing of aluminium-copper alloys. *Transactions of the Metallurgical Society of AIME*, 1967, **239**, 1504–1511.
20. Wilson, P. W., Kattamis, T. Z. and Shiohara, Y., Coarsening during solidification of aluminium-copper alloys. *Journal of Material Science*, 1988, **23**(18), 2882–2892.
21. Thevik, H. J. and Mo, A., The effect of coarsening upon macrosegregation close to a cast surface. In *Modeling of Casting, Welding and Advanced Solidification Processes VII*, eds M. Cross and J. Campbell. Warrendale, PA, 1995, TMS, pp. 557–564.
22. Thevik, H. J., Mathematical modelling of macrosegregation formation close to a cast surface. PhD thesis, University of Oslo, Norway, 1996.
23. *MATLAB User's Guide*. The MathWorks, Inc., Natick, MA 01760, 1992.
24. Kato, H. and Cahoon, J. R., Inverse segregation in directionally solidified Al–Cu–Ti alloys with equiaxed grains. *Metallurgical Transactions*, 1985, **16A**, 579–587.
25. Ganesan, S. and Poirier, D. R., Densities of aluminum-rich aluminum–copper alloys during solidification. *Metallurgical Transactions*, 1987, **18A**, 721–723.
26. Voller, V. R., Department of Civil Engineering, University of Minnesota, MI. Private communication, 1995.
27. Sundarraj, S. and Voller, V. R., Effects of microscale phenomena and density in modelling macrosegregation. In *Modeling of Casting, Welding and Advanced Solidification Process VII*, eds M. Cross and J. Campbell. Warrendale, PA, 1995, TMS, pp. 131–138.
28. Jensen, E. K., Mathematical model calculations in level pour DC-casting of aluminium extrusion ingots. In *Light Metals*, ed. K. J. McMinn. Warrendale, PA, 1980, TMS-AIME, pp. 631–642.
29. Rappaz, M. and Voller, V., Modelling of micro-macrosegregation in solidification processes. *Metallurgical Transactions*, 1990, **21A**, 749–753.
30. Poirier, D. R., Nandapurkar, P. J. and Ganesan, S., The energy and solute conservation equations for dendritic solidification. *Metallurgical Transactions*, 1991, **22B**, 899–900.
31. Pehlke, R. D., Jeyarajan, A. and Wada, H., Summary of thermal properties for casting alloys and mold materials. Technical report PB83-211003, National Technical Information Service, 1983.
32. Murphy, J. B., Interdiffusion in dilute aluminium–copper solid solutions. *Acta Metallurgica*, 1961, **9**, 563–569.
33. Dean, N. F., Mortensen, A. and Flemings, M. C., Microsegregation in cellular solidification. *Metallurgical and Materials Transactions*, 1994, **25A**, 2295–2301.
34. Massalski, T. B. (ed.), *Binary Alloy Phase Diagrams*, Vol. 1, ASM International, 2nd edn, 1990.
35. Gündüz, M. and Hunt, J. D., *Acta Metallurgica*, 1985, **33**, 1651–1672.